Dimer interaction in the Hv1 proton channel

Laetitia Mony[a,b], David Stroebel[b], and Ehud Y. Isacoff[a,c,d,1]

[a]Department of Molecular and Cell Biology, University of California, Berkeley, CA 94720; [b]Institut de Biologie de l'Ecole Normale Supérieure, CNRS UMR 8197, INSERM U1024, Ecole Normale Supérieure, Paris Sciences et Lettres Research University, 75005 Paris, France; [c]Helen Wills Neuroscience Institute, University of California, Berkeley, CA 94720; and [d]Bioscience Division, Lawrence Berkeley National Laboratory, Berkeley, CA 94720

Contributed by Ehud Y. Isacoff, July 9, 2020 (sent for review May 19, 2020; reviewed by H. Peter Larsson and Riccardo Olcese)

The voltage-gated proton channel Hv1 is a member of the voltage-gated ion channel superfamily, which stands out in design: It is a dimer of two voltage-sensing domains (VSDs), each containing a pore pathway, a voltage sensor (S4), and a gate (S1) and forming its own ion channel. Opening of the two channels in the dimer is cooperative. Part of the cooperativity is due to association between coiled-coil domains that extend intracellularly from the S4s. Interactions between the transmembrane portions of the subunits may also contribute, but the nature of transmembrane packing is unclear. Using functional analysis of a mutagenesis scan, biochemistry, and modeling, we find that the subunits form a dimer interface along the entire length of S1, and also have intersubunit contacts between S1 and S4. These interactions exert a strong effect on gating, in particular on the stability of the open state. Our results suggest that gating in Hv1 is tuned by extensive VSD–VSD interactions between the gates and voltage sensors of the dimeric channel.

voltage-gated channel | ion channel | proton channel | Hv1

Intracellular pH of the cell is tightly regulated by intracellular buffers, proton transporters, and proton channels (1). At the plasma membrane, voltage-gated proton channels (Hv1) act as dynamic regulators of intracellular pH by mediating proton extrusion from the cytoplasm following membrane depolarization or intracellular medium acidification (2). These channels, which are expressed in a wide range of species and tissues (2), play a particularly important role in the immune system. There they compensate intracellular acidification induced by NADPH oxidase activity during the immune response, thereby sustaining the production of reactive oxygen species (3–6). Because of this mechanism, Hv1 activation in the microglia was shown to be associated with increased brain damage after ischemic stroke (7). Up-regulation of Hv1 expression and activity was furthermore found in metastatic human breast cells (8) and malignant B cells (9), making of Hv1 a potential target for cancer treatment. Finally, by allowing maturation of sperm cells through alkalinization of their cytoplasm, Hv1 is also likely to play a major role in the control of male fertility (10). Hv1 channels are thus potential targets of therapeutic interest. However, lack of specific pharmacology has so far impeded their targeting in the clinic.

Hv1 channels are peculiar members of the superfamily of voltage-gated cation channels (VGIC). "Classic" members are tetramers, each subunit containing a four-transmembrane-segment (S1–S4) voltage-sensing domain (VSD), and a two-transmembrane-segment (S5–S4) pore domain, which contributes one-quarter of the pore, forming a channel with four voltage sensors and a central pore (11). In contrast, Hv1 channels assemble as dimers (12–14), whose subunits are solely composed of a VSD (15, 16). Each subunit contains its own voltage-sensor, gate, and pore and can function autonomously (12, 13, 17, 18). The architecture and the mechanism of gating of the protomer are starting to be elucidated. The S1 and S4 segments were identified as the principal elements of gating. As in other VGICs, S4 is the voltage sensor in Hv1 (18–20). S1 was proposed as the gate (21). And both S1 and S4 were shown to contribute to the selectivity filter composed of D1 (D112 in human Hv1 [hHv1]) in S1 and of the third arginine (R3) of the S4 segment (22, 23). A crystal structure of a chimera between mouse Hv1 (mHv1) and *Ciona intestinalis* voltage-sensing phosphatase (CiVSP) (mHv1cc) (24) and a recent NMR structure of an hHv1 VSD (25) have provided insights on the structure of Hv1 closed states. However, the exact architecture of the Hv1 dimer has been elusive. It is known that Hv1 subunits assemble intracellularly via a C-terminal coiled-coil domain, which is necessary and sufficient for dimerization (12, 13), although efficiency of dimerization is increased by the N-terminal domain (12, 13). The coiled-coil domain, which is in direct continuity with the S4 helix (26), induces cooperative gating of the channel subunits, resulting in slowing of channel opening and closure compared to the monomer (20, 27, 28). The arrangement of the transmembrane portion of the VSDs in the dimer is under debate. Based on cross-linking studies and in in silico dimer reconstruction using the crystal structures of mHv1cc monomers (24) and the dimeric Hv1 coiled-coil domain (28), the Okamura group proposed that the VSDs interact mainly via their S4 segments (24, 29) (S4–S4 model). Counterposed to this, based on cross-linking between the extracellular ends of the S1 segments (14) and the crystal structure of a dimer of CiVSP VSDs (30), Li et al. (31) proposed that Hv1 VSDs interact through both their S1 and S4 segments (S1–S4 model). Whatever the exact nature of the TMD interactions, they have been shown to mediate cooperativity that changes the structure of the channel in such a way as to alter pore blocker pharmacology (32), but the role of transmembrane dimer interactions in Hv1 gating is still largely unknown.

To date, the architecture of Hv1 dimer interface has been investigated biochemically on purified channels in detergent or in isolated membranes (14, 26, 31). In this report, we used a functional assay on full-length Hv1 channels in intact cells to determine the contribution of the S1 segment to the dimer interface. We found that not only the extracellular end, but the full length of S1 participates in the transmembrane interface, providing experimental validation of the S1–S4 model. Our work

Significance

The Hv1 proton channel is an unusual voltage-gated ion channel with atypical architecture and stoichiometry. While functional as a monomer, Hv1 is usually expressed as a dimer of two voltage-sensing domains (VSDs). How the two VSDs arrange relative to each other is a matter of debate and the functional impact of VSD–VSD interactions is only partly understood. We show that the Hv1 dimer interface is formed by the S1 and S4 transmembrane segments of the VSD. We find this S1–S4 dimer interface to be a strong regulator of Hv1 gating. This interface therefore constitutes a promising target for the development of allosteric modulators for this class of channels critical for pH regulation and immunity.

Author contributions: L.M. and E.Y.I. designed research; L.M. and D.S. performed research; L.M., D.S., and E.Y.I. analyzed data; and L.M. and E.Y.I. wrote the paper.

Reviewers: H.P.L., University of Miami; and R.O., University of California, Los Angeles.

The authors declare no competing interest.

[1]To whom correspondence may be addressed. Email: ehud@berkeley.edu.

This article contains supporting information online at https://www.pnas.org/lookup/suppl/doi:10.1073/pnas.2010032117/-/DCSupplemental.

First published August 11, 2020.

identifies the transmembrane dimer interface as a strong regulatory element of Hv1, suggesting pharmacological target for regulating the function of Hv1.

Results

Scanning the S1 Segment for Interfacial Residues. The nature of Hv1 dimer interface was previously investigated biochemically using cysteine–cysteine cross-linking in proteins purified in detergent or reconstituted into artificial bilayers (14, 26). In the absence of a dimer structure, cysteine pairs were introduced based on guesses about contact sites. Furthermore, the function of the cysteine mutants was not tested, leaving it possible that some of the cross-links that did form might have occurred in misfolded, nonfunctional channels. To overcome these limitations, we designed an unbiased screen for interfacial residues based on the functional characterization of full-length channels in intact cells. We performed a mutant scan, where cysteine was substituted at many individual positions, and we measured the impact of the mutation on channel function and compared that impact between dimeric and monomerized Hv1 (Fig. 1). Our expectation was that mutation of residues that lie on a protein–protein interface will have a high impact on function, while mutation of those that face lipid will have a low impact.

Residues in the Hv1 transmembrane helices can be conceptually divided into three groups: 1) Residues pointing toward the inside of the VSD (positions a and e in Fig. 1*A*); 2) residues pointing toward the outside of the VSD in the direction of the lipid bilayer (positions c and d in Fig. 1*A*); and 3) residues pointing toward the outside of the VSD in the direction of the dimer interface (position b in Fig. 1*A*). In the dimer, mutation of residues facing the lipid bilayer (positions c and d) should have little impact on function, whereas mutation of residues facing protein (positions a, b, and e) should substantially perturb function (33, 34). Monomerization of the channel will leave residues at positions a and e facing protein and c and d facing lipid, and therefore the mutations will have the same effect that they do in the dimer. In contrast, residues at position b will point into the lipid and lose their protein interaction when the channel is monomerized. Consequently, mutation there should have little impact on function in the monomer (Fig. 1*A*). This last set of residues, whose mutation impacts function only in the dimer, thus lie at the dimer interface. This paradigm is true if the residue at position b points away from the core of the VSD in all functional states. If it happens to alternate between intra- and inter-VSD orientations, or if the cysteine mutation perturbs the local protein structure, its mutation could have a strong impact in both monomer and dimer backgrounds. In that case, additional experiments of disulfide cross-linking will be required to assess the interfacial property of that residue.

We individually mutated each S1 residue of *C. intestinalis* Hv1 (CiHv1), from I149 to I175, into a cysteine, either in the background of the WT, dimeric CiHv1, or of a monomeric CiHv1 in which the N and C termini were truncated (Δ*N*-CiHv1-ΔC) (12). Each construct was characterized by two-electrode voltage clamp (TEVC) on *Xenopus* oocytes. We used an Hv1 from *C. intestinalis* due to its higher expression and left-shifted conductance-voltage (*G-V*) curve compared to vertebrate Hv1, thus allowing reliable recordings in *Xenopus* oocytes. The strong sequence homology between the transmembrane domains of CiHv1 and its vertebrate orthologs suggests common assembly and gating mechanisms (16). We collected the $V_{1/2}$ and slope of their *G-V* curves, as well as the kinetics of activation and deactivation (see examples in *SI Appendix*, Fig. S1), and considered that the function of the channel was altered by the cysteine mutation when at least one of the parameters was changed by a certain threshold amount compared to the control channel (dimeric CiHv1wt or monomeric Δ*N*-CiHv1-ΔC) (Table 1; see *Methods* for the determination of a threshold change).

Results of the cysteine scanning are summarized in Fig. 1*B* and Table 1. When mapped on a helical wheel, perturbations of the extracellular half of S1 (D160 and up) clearly segregated into three quadrants: Residues with little impact in both dimer and monomer (Fig. 1*C*, gray), likely facing the lipids; residues impacting both the dimer and monomer (Fig. 1*C*, red and pink), likely facing the VSD interior; and residues impacting the dimer, but not the monomer (Fig. 1*C*, blue), likely facing the dimer interface. This is indicative of a tight packing, especially in the most upper part (E167 to D171), where cysteine substitution of all positions had a strong impact in both the dimer and the monomer (Fig. 1 *B* and *C* and Table 1). Intracellularly, cysteine mutations had overall much less impact, with six positions showing little impact in both monomer and dimer, three positions showing impact in the dimer only, and only one mutation showing impact in both dimer and monomer, indicative of a looser packing. These findings are consistent with the X-ray structure of the mHv1cc construct, which flares out intracellularly (24).

Overall, in 7 of the 27 tested positions the cysteine mutation altered the function of the dimeric channel, but not of the monomeric channel (in blue in Fig. 1 *B* and *C*). Residues at the external tip of S1, such as L172 and K173, which were shown earlier to cross-link in hHv1 and mouse Hv1 (mHv1) (14, 26) were among the seven residues with impact only in the dimeric channel, validating the logic of our assay. These putative interfacial residues were not restricted to the external tip of S1, as previously thought (14, 26), but extended through its entire length (Fig. 1*B*). Our assay therefore suggests that the S1 segment makes extensive contacts with the partner subunit with both its extracellular and intracellular sides. However, since our functional assay is an indirect measure of interprotomer interaction, we set out to validate the interfacial character of the highlighted residues, investigate their functional impact, and identify their potential partners.

Architecture of the Transmembrane Hv1 Dimer Interface. To validate the results of our functional assay and obtain structural insights on the location of the dimer interface, we first mapped our results onto homology models of CiHv1 isolated protomers using either the X-ray structure of a mHv1cc VSD [PDB ID code 3WKV (24)] or the NMR structure of hHv1 VSD [PDB ID code 5OQK (25)] as templates (*SI Appendix*, Fig. S2). In both homology models, residues of the external half of S1 (D160 and up) mapped according to the effect of their perturbation: Residues impacting both dimer and monomer facing the inside of the VSD (Fig. 1*C*, pink quadrant), and residues with little impact or impacting only the dimer facing outside the VSD (Fig. 1*C*, gray and blue quadrants, respectively). Extracellular putative interfacial residues (i.e., S161, V165, L172, and K173, named "Interface I" hereafter) were all located on the same face of the S1 helix, and pointed toward previously identified S4 interfacial residues (26) (Fig. 1 *D–G*). This suggests that these residues form a common dimerization interface with S4 interfacial residues. In contrast, S1 intracellular putative interfacial residues (I149, H150, and I153, Interface II) mapped to the inner VSD quadrant according to the mHv1cc-based homology model (3WKV-based model) (Fig. 1 *C, D,* and *F*), facing toward the same direction as selectivity filter residue D160. In the OQK-based model, however, arrangement of the transmembrane segments was completely different. Alignment of the two homology models based on the S1 and S2 segments gave the best results and revealed a large and upward swinging of an S3–S4 paddle when going from the 3WKV-based to the OQK-based model (*SI Appendix*, Fig. S2 *B* and *C*). This large rearrangement moved the inner half of S1, allowing I149, H150, and I153 to face the outside of the VSD (Fig. 1 *E* and *G*). The NMR structure obtained for hHv1 VSD was attributed to a closed, yet more activated state than mHv1cc X-ray structure (25). Results of our perturbation assay are therefore in agreement with the

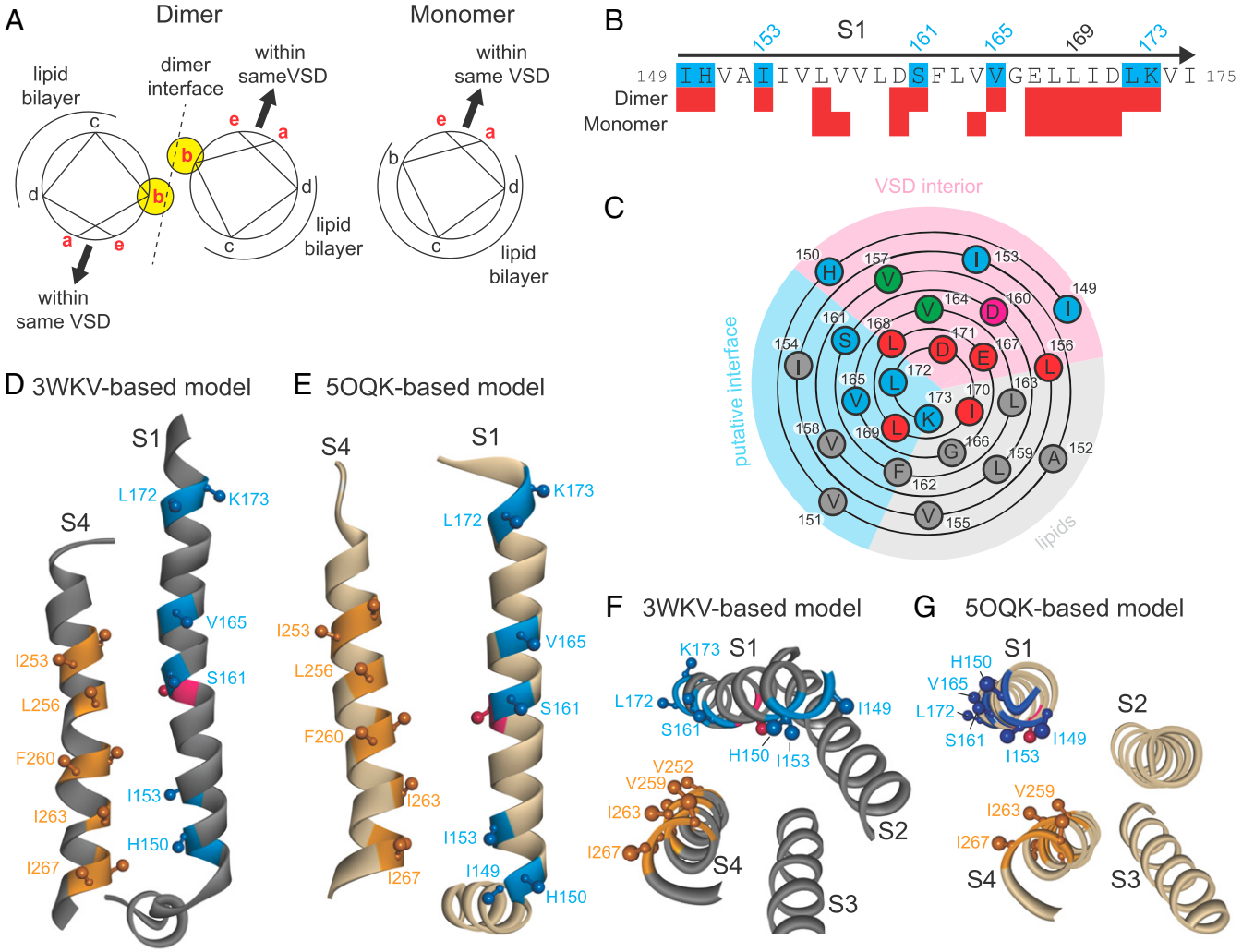

Fig. 1. Identification of S1 interfacial residues with a functional cysteine scanning assay. (*A*) Principle of the perturbation scanning assay to identify interfacial positions in transmembrane α-helices. Positions facing a protein environment are depicted in red. Interfacial positions are circled in yellow. (*B*) Summary of the functional cysteine scanning assay. Residues whose cysteine mutation loses its effect with monomerization are highlighted in blue. Red squares represent residue positions for which cysteine mutation significantly perturbs channel function, either in the dimeric or monomeric background. We could not measure any proton current for either dimeric or monomeric channels containing the D160C mutation, so we considered that this mutation perturbed Hv1 function in both the dimer and the monomer. (*C*) Wengxiang diagram of S1 helix with residue positions color-coded as follows: Gray, low impact in both dimer and monomer; red, high impact in both dimer and monomer; pink, selectivity filter D160, also high impact in both dimer and monomer (no current); green, low impact in dimer and high impact in monomer; blue, high impact in dimer and low impact in monomer (putative interface). Limits of the different quadrants (VSD interior, lipids, and putative interface) were determined according to CiHv1 3WKV-based model (see below). (*D*–*G*) Mapping of S1 putative interfacial positions found with our functional assay (blue) onto homology models of CiHv1 VSD using either the X-ray structure of the mHv1-CiVSP chimera (24) (3WKV-based model, gray backbone), or the NMR structure of an hHv1 VSD (25) (5OQK-based model, beige backbone), as templates. (*D* and *E*) Side view, S2, and S3 segments were removed for clarity. (*F* and *G*) Bottom view. Selectivity filter D160 (pink) points toward the inside of the VSD. S4 interfacial positions previously found by cross-linking (26) are represented in orange. Small and big balls represent the positions of the α- and β-carbons, respectively, of the residues of interest. Note the good alignment of our putative S1 interfacial residues with S4 interfacial positions.

available structures of isolated Hv1 VSDs, and suggest that intracellular residues I149, H150, and I153 might alternate between an intra-VSD and an interfacial orientation, depending on the gating state (Fig. 1 *F* and *G* and *SI Appendix*, Fig. S2*D*).

We next modeled an Hv1 dimer. As previously done (26, 29), we artificially created an Hv1 dimer template by aligning the GCN4 coiled-coil domains of two mHv1cc monomers (24) (PDB ID code 3WKV) with the structure of the dimeric coiled-coil domain of mHv1 (28) (PDB ID code 3VMX). However, in previous studies (26, 29), such alignment (Alignment 1 in *SI Appendix*, Fig. S3*A*) resulted in an arrangement of the VSDs in which S4 forms the vast majority of the dimer interface, with little involvement of the other segments (*SI Appendix*, Fig. S3*B*). This is not compatible both with our current results and with most published cross-linking data on S1 (14) and S4 (26). For example, the tryptophan at position 257 (203 in mHv1), which faces its cognate in the other protomer in this VSD arrangement (*SI Appendix*, Fig. S3*B*), when mutated into cysteine cross-links minimally (26). This mismatch between functional and biochemical data on the one hand and the structural model on the other hand may arise from a distortion of the helicity of the S4 segment around R261 (R3) in the crystal structure, which results in a wrong arrangement of the transmembrane segments when the GCN4 and mHv1 coiled-coils are aligned. To compensate for this distortion, we structurally aligned the coiled-coil domains so that S4

Table 1. Gating parameters of S1 cysteine mutants

	Dimer					Monomer				
Mutation	$\Delta V_{1/2}$ (mV)	ΔB (mV)*	Mutant/WT, On kinetics†	Mutant/WT, Off kinetics‡	*n*	$\Delta V_{1/2}$ (mV)	ΔB (mV)*	Mutant/WT, On kinetics†	Mutant/WT, Off kinetics†	*n*
I149C	**−16 ± 6**	**−8 ± 1**	**3.6 ± 0.5**	0.9 ± 0.3	14	−2 ± 5	−2.3 ± 0.4	1.4 ± 0.3	1.40 ± 0.05	6
H150C	**−39 ± 3**	**−8 ± 1**	0.5 ± 0.1	1.4 ± 0.2	10	4 ± 5	5 ± 3	1.2 ± 0.1	1.6 ± 0.2	3
V151C	3 ± 6	−1.9 ± 0.7	2 ± 1	1.3 ± 0.1	5	−10 ± 5	−1 ± 1	0.8 ± 0.2	0.91 ± 0.08	9
A152C	−8 ± 4	−4 ± 1	1.3 ± 0.4	0.65 ± 0.08	10	−2 ± 4	3 ± 1	0.8 ± 0.1	0.74 ± 0.09	10
I153C	**−67 ± 2**	**−9 ± 1**	**0.26 ± 0.01**	0.6 ± 0.2	4	−11 ± 6	**13 ± 4**	0.98 ± 0.05	0.75 ± 0.07	11
I154C	−8 ± 5	−0.6 ± 0.9	1.0 ± 0.2	2.7 ± 0.4	17	−0.2 ± 2	−1.3 ± 1.5	0.95 ± 0.05	1.1 ± 0.1	14
V155C	−6 ± 4	−0.01 ± 0.35	0.82 ± 0.09	1.5 ± 0.2	4	0 ± 3	0.4 ± 0.5	0.96 ± 0.08	1.2 ± 0.1	9
L156C	**−12 ± 5**	−2 ± 1	1.4 ± 0.3	1.1 ± 0.2	10	**−19 ± 2**	−3 ± 1	0.76 ± 0.08	1.1 ± 0.2	6
V157C	−7 ± 6	−2.8 ± 0.8	1.6 ± 0.3	1.9 ± 0.3	10	**−37 ± 4**	**−11.1 ± 0.3**	0.57 ± 0.02	0.89 ± 0.09	6
V158C	−8 ± 3	−2.5 ± 0.7	0.85 ± 0.09	0.7 ± 0.1	10	−2 ± 2	−3.7 ± 0.6	0.64 ± 0.02	0.74 ± 0.02	6
L159C	4 ± 6	−0.2 ± 0.5	2.6 ± 0.7	2.2 ± 0.4	8	−2 ± 4	−2.0 ± 0.8	0.78 ± 0.09	0.82 ± 0.02	6
D160C	n.d.§	n.d.§	n.d.§	n.d.§		n.d.§	n.d.§	n.d.§	n.d.§	
S161C	**−25 ± 6**	1 ± 1	**0.38 ± 0.08**	**25 ± 6**	10	10 ± 1	−4 ± 1	1.2 ± 0.2	0.81 ± 0.04	12
F162C	1 ± 3	0 ± 1	1.8 ± 0.3	1.8 ± 0.3	3	−1 ± 3	−2.9 ± 0.7	0.79 ± 0.07	1.00 ± 0.05	6
L163C	−4 ± 2	0 ± 1	1.2 ± 0.2	1.3 ± 0.2	3	10 ± 1	−4 ± 1	1.1 ± 0.2	0.93 ± 0.04	6
V164C	5 ± 3	−1 ± 1	3 ± 1	0.7 ± 0.1	6	**−14 ± 1**	**−7 ± 1**	1.35 ± 0.07	1.39 ± 0.03	6
V165C	**−16 ± 7**	1.3 ± 0.8	4 ± 2	**12 ± 3**	11	4 ± 3	−3 ± 1	0.87 ± 0.09	1.03 ± 0.05	6
G166C	11 ± 5	1 ± 1	2.2 ± 0.7	1.5 ± 0.3	6	2 ± 7	**−7 ± 1**	1.5 ± 0.7	0.93 ± 0.09	5
E167C	**34 ± 6**	1.6 ± 0.6	**23 ± 11**	0.89 ± 0.09	6	**18 ± 6**	−3 ± 2	**5 ± 1**	**3.0 ± 0.6**	5
L168C	**−35 ± 9**	−3 ± 1	**0.17 ± 0.04**	**0.21 ± 0.02**	4	**−42 ± 3**	−3 ± 3	0.68 ± 0.07	1.00 ± 0.05	6
L169C	**−23 ± 4**	2 ± 1	0.7 ± 0.9	**5.0 ± 0.8**	24	**−18 ± 6**	3 ± 1	0.68 ± 0.08	**2.5 ± 0.2**	10
I170C	**26 ± 4**	−3 ± 2	3 ± 1	**0.36 ± 0.06**	6	**−30 ± 3**	**−6 ± 2**	0.81 ± 0.06	1.14 ± 0.05	6
D171C	**41 ± 3**	4 ± 1	1.7 ± 0.2	**0.15 ± 0.01**	6	**−35 ± 2**	**32 ± 5**	**13 ± 2**	**5 ± 1**	6
L172C	**33 ± 3**	−5 ± 2	3 ± 1	**0.13 ± 0.02**	6	0 ± 2	−2 ± 1	1.2 ± 0.1	1.83 ± 0.09	6
K173C	**−26 ± 5**	2.0 ± 0.8	0.49 ± 0.06	**3.0 ± 0.4**	16	−4 ± 4	−1 ± 1	1.6 ± 0.2	1.2 ± 0.1	6
V174C	0 ± 1	−0.6 ± 0.4	0.87 ± 0.07	0.70 ± 0.05	16	2 ± 5	−1 ± 1	1.7 ± 0.2	1.22 ± 0.03	6
I175C	−2 ± 2	−1.1 ± 0.5	1.0 ± 0.1	0.68 ± 0.07	18	10 ± 2	2 ± 1	1.4 ± 0.2	1.5 ± 0.1	6

Gating parameters affected by a threshold amount compared to WT channels (±10 mV for $\Delta V_{1/2}$, ±5 mV for ΔB, threefold for on and off kinetics; see *Methods*) are highlighted in bold. Positions at which a cysteine mutation has impact (threshold change of at least one gating parameter) in the dimer but not in the monomer are also highlighted in bold. *n* = number of cells.

*B represents the Boltzmann factor kT/ze_0. The smaller B, the steeper the G-V curve.

†Ratio of the weighted time constants.

‡Ratio of the 90% to 10% decay times.

§n.d., not determined, due to the absence of proton currents in oocytes expressing CiHv1-D160C and Δ*N*-CiHv1-D160C-ΔC channels.

residues that were shown to cross-link minimally (positions corresponding to CiHv1-L254, -W257, -R258, -R261, -I262, and -G265) (26) face away in the dimer template (*SI Appendix*, Fig. S3*D*). This yielded a dimer template involving both S1 and S4 segments, similarly to the dimer model proposed by Li et al. (31), which was based on a crystal structure Ci-VSP VSD that crystallized as a dimer in the asymmetric unit (30). From this structural alignment, we derived a sequence alignment between CiHv1 and the two template structures (*SI Appendix*, Fig. S3*F*) that we used to build a homology model of a CiHv1 dimer. The structural model of the CiHv1 dimer is shown in Fig. 2. At the very extracellular end (Region I in Fig. 2), the dimer interface was formed by the external tips of the two S1 segments, the two residues I175 (I127 in hHv1) being the closest, consistent with previously published biochemical data (14) (Fig. 2 *A* and *D*). Deeper in the membrane, the dimer interface involved both S1 and S4, with the S4 segment of one protomer interacting with both S1 and S4 segments of the other protomer (Fig. 2). In particular, the face of the S1 helix encompassing Interface I residues directly contacted the other protomer through S1–S4 interactions (Fig. 2, Region II). Finally, the intracellular side of the dimer interface was mostly formed by S4–S4 interactions (Fig. 2*D*, Region III). As expected from the design of our dimer template, the vast majority of the S4 residues previously shown to crosslink (26) did face each other in this model (Fig. 2*D*, Region III).

The dimer interface formed by S1 also included L169, which completes the helical pattern made by Interface I residues (see below). L169 did not come out in our assay because its mutation changed function in both the dimer and monomer. It is indeed located in the high impact S1 region (E167 to D171) described above. Cysteines introduced at position L169 were shown to weakly cross-link between protomers (14, 26), suggesting that this residue can face the dimer interface. Similarly to Interface II (internal) residues, L169 might be able to alternate between intra- and interprotomer orientations, depending on the gating state. Alternatively, mutation of L169 into a cysteine may slightly distort the S1 helix and change the position of the two flanking acidic residues (E167 and D171), which influence channel function in both the dimer and monomer and have been proposed to control S4 conformational changes (35, 36).

To test the interpretation that position L169 lies at the dimer interface and validate the S1–S4 interface model, we introduced a cysteine at L169 in the S1 segment of one protomer and paired this with a cysteine at one of several positions in the S4 segment of the other protomer that face L169 in the structural dimer model. We then determined whether the cysteines would form a disulfide cross-link by Western blot analysis. We were not able to perform this analysis in CiHv1, since it forms dimers under reducing conditions (*SI Appendix*, Fig. S4*A*). We therefore turned to a GFP-tagged, human Hv1 (hHv1) construct in which the endogenous cysteine C249 was mutated to an alanine to avoid background cross-linking (hHv1*-GFP) (14, 31). Hv1 proteins were detected by immunoblotting with an antibody against GFP.

PHYSIOLOGY

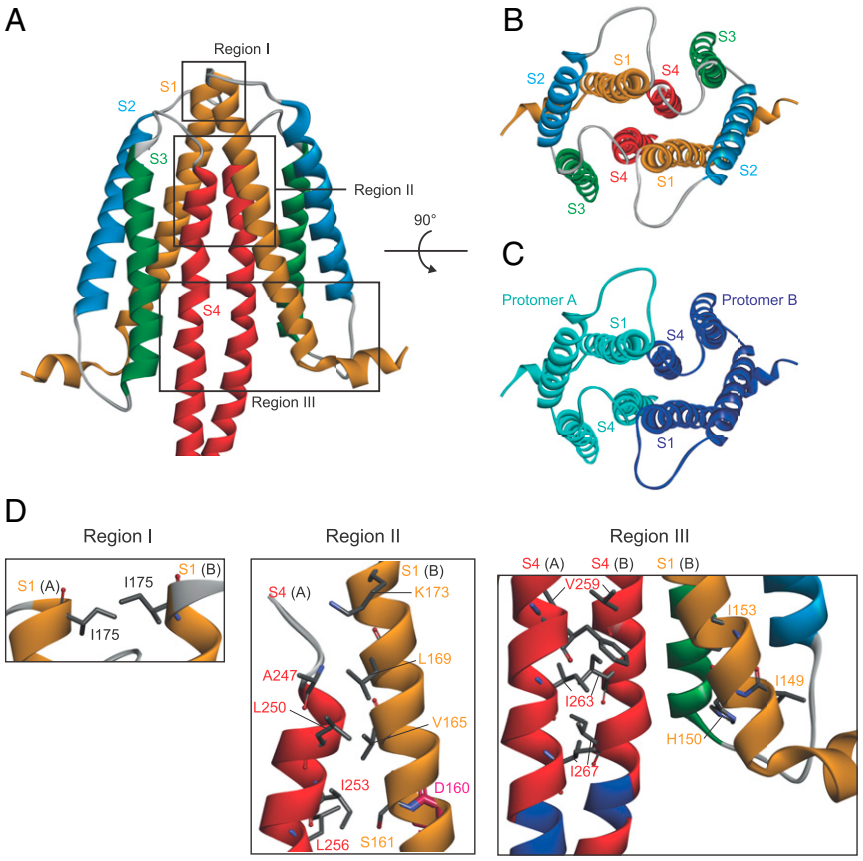

Fig. 2. Homology model of CiHv1 dimer. (*A*) Side view of the transmembrane segments of the CiHv1 dimer model. Transmembrane segments are depicted as follows: S1, orange; S2, blue; S3, green; and S4, red. Loops are depicted in white. Black rectangles delimit regions of interest at the level of the dimer interface. (*B* and *C*) CiHv1 dimer model viewed from its extracellular face. (*B*) Same color code as in *A*. (*C*) Each protomer is represented in a different color (cyan for protomer A and dark blue for protomer B) to highlight their relative arrangement. (*D*) Close-up view of the regions of interest highlighted in *A*. Same color code as in *A* for the transmembrane helices. The identity of the protomer (A or B) is indicated in parenthesis after the name of the transmembrane segment. S1 interfacial residues and their putative partners on the neighbor subunit are shown as sticks. In the Region II *Inset*, segments other than S4 (A) and S1 (B) have been removed for clarity. D160 is shown as pink sticks to mark the middle of the S1 segment. In the Region III *Inset*, the linker between S4 and the coiled-coil segment is colored in dark blue.

Based on our homology model, CiHv1-L169 (hHv1-I121) on S1 is expected to interact with CiHv1-A247, G249, and L250 (hHv1-A197, G199, and L200) on S4 (Fig. 2*D*, Region II). To differentiate cross-linking between S1 and S4 segments (heterodimer) from potential cross-linking between the same residue in each protomer (S1–S1 or S4–S4, homodimer), we coexpressed in *Xenopus* oocytes a GFP-tagged hHv1* subunit containing the S1 mutation I121C (hHv1*-I121C-GFP) with an untagged control (WT*) or with one of three variants containing a cysteine mutation on S4 (hHv1*-A197C, G199C, or L200C), thus allowing us to distinguish homodimers from the heterodimer based on molecular weight (homodimer of hHv1*-I121C-GFP would be biggest because of its two GFPs; homodimer of hHv1*-A197C, G199C or L200C would not be detected because of no GFP; heterodimer

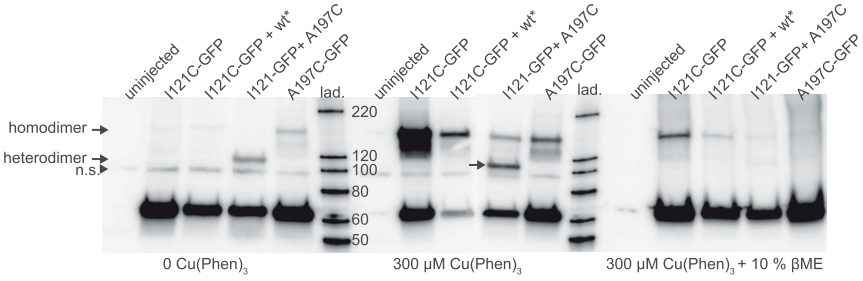

Fig. 3. Validation by Western blot analysis of the transmembrane dimer interface. Immunoblots from *Xenopus* oocytes expressing hHv1*-I121C-GFP, hHv1*-A197C-GFP, or coexpressing hHv1*-I121C-GFP with untagged hHv1* (wt*) or hHv1*-A197C, and revealed with an anti-GFP antibody. Proteins were either purified from untreated [0 $Cu(Phen)_3$] (*Left*) oocytes, or oocytes submitted to an oxidative treatment (*Center* and *Right*). In the latter case, purified proteins were either denatured in nonreducing [300 μM $Cu(Phen)_3$] (*Center*) or reducing conditions [300 μM $Cu(Phen)_3$ + 10% βME] (*Right*). The arrow indicates the heterodimer band formed by cross-linking of I121C and A197C. n.s., nonspecific band that is also present in oocytes that do not express hHv1 (uninjected condition). lad., ladder.

of hHv1*-I121C-GFP with hHv1*-A197C, G199C, or L200C would be intermediate in size with one GFP) (Fig. 3 and *SI Appendix*, Fig. S4*B*). Expressing oocytes were either left untreated or incubated in the oxidative agent copper phenanthroline [$Cu(Phen)_3$], then thoroughly washed before cell lysis. Contrary to previous studies in which $Cu(Phen)_3$ treatment was performed on purified proteins or membrane extracts (14, 26), our experimental protocol ensures that the observed dimers were formed from mature, plasma membrane-expressed channels (37).

We confirmed that on its own I121C cross-linked with its cognate partner on the other protomer (I121C/I121C homodimers) under oxidizing conditions, as shown by the ~160-kDa homodimer band, which was strongly decreased under reducing conditions (Fig. 3). The same was true for A197C (Fig. 3). When hHv1*-I121C-GFP was coexpressed with untagged hHv1*-A197C (but also, to a lesser extent, with hHv1*-G199C and -L200C) (*SI Appendix*, Fig. S4*C*), an additional band appeared at lower molecular mass (~110 kDa) (Fig. 3). This band was not present when hHv1*-I121C-GFP was

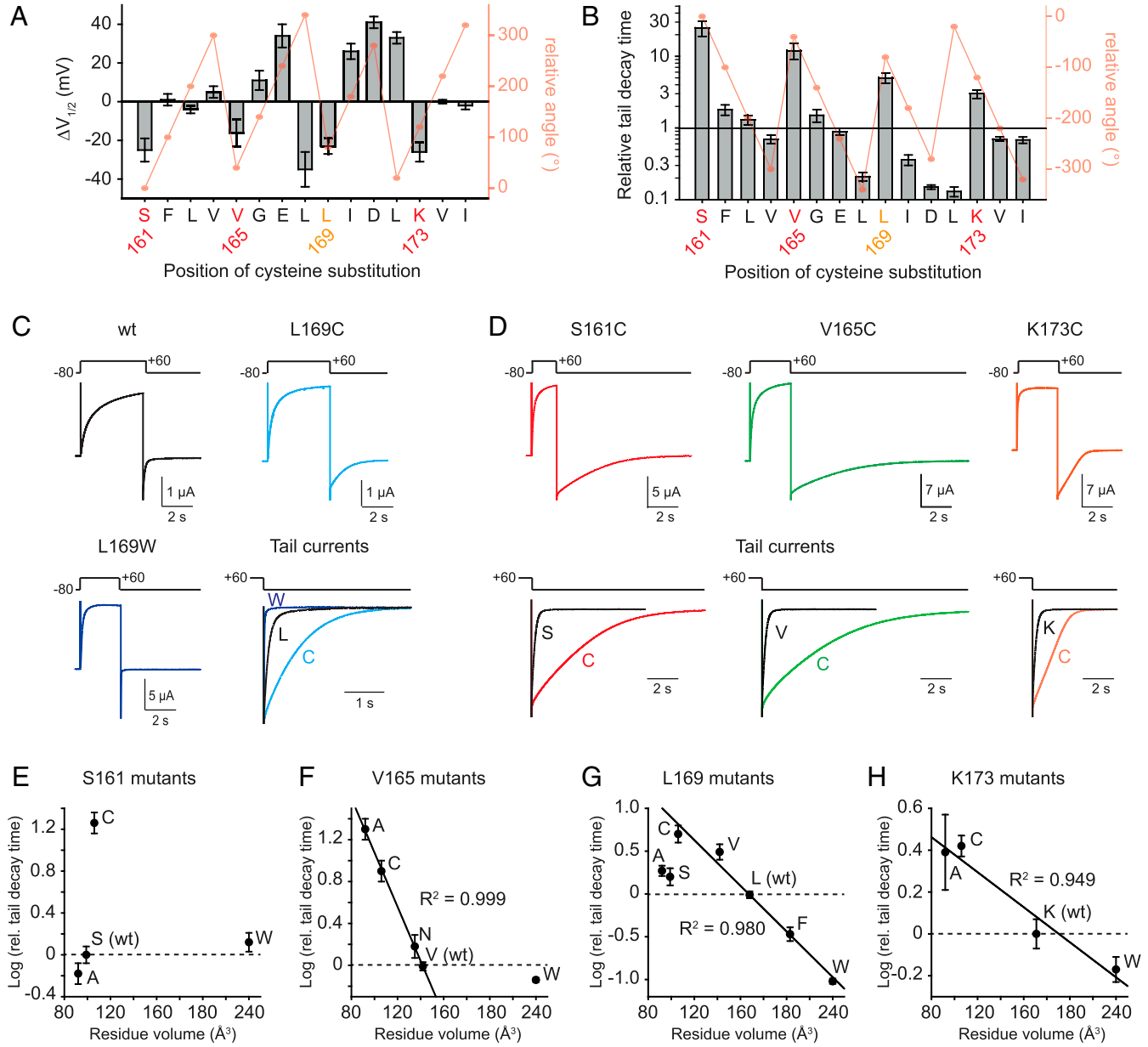

Fig. 4. Steric hindrance between residues of the transmembrane dimer interface drives channel closure kinetics. (*A* and *B*) Shifts of $V_{1/2}$ ($\Delta V_{1/2}$, *A*) and relative tail decay times (*B*) between WT channels and channels containing a cysteine mutation in S1 external half (S161 to I175). Superimposed in red are the theoretical orientation angles between the α-carbons of the given residue and S161 (taken as the reference), considering that these residues belong to an α-helix. Note that cysteine mutations at positions with orientations close to S161 specifically lead to leftward shifts of the *G-V* curve ($\Delta V_{1/2} < 0$) and slowing of channel closure. (*C*) Representative current traces for a voltage step to +60 mV of oocytes expressing CiHv1 channels mutated at position L169 and superposition of their normalized tail currents. (*D*) Current traces of other Interface I residues (*Upper*) and superposition of the normalized WT and mutant tail currents (*Lower*). (*E–H*) Relative tail decay times as a function of the volume of the residue (50) introduced at positions S161 (*E*), V165 (*F*), L169 (*G*), and K173 (*H*). Note the linear relationship (black line) between the log of the relative tail decay time and the volume of the introduced residue at positions V165, L169, and K173. Mutants L169A, L169S, and V165W were excluded from the linear fits. The dashed line indicates no effect on the tail decay time. Total numbers of oocytes: WT, 4; CiHv1-S161A, 12; CiHv1-S161C, 13; CiHv1-S161W, 5; CiHv1-V165A, 9; CiHv1-V165C, 5; CiHv1-V165N, 5; CiHv1-V165W, 6; CiHv1-L169A, 6; CiHv1-L169S, 17; CiHv1-L169C, 6; CiHv1-L169V, 6; CiHv1-L169F, 5; CiHv1-L169W, 12; CiHv1-K173A, 12; CiHv1-K173C, 16; CiHv1-K173W, 6.

expressed with hHv1* ("wt") and disappeared in reducing conditions. It thus represents the heterodimer made by the cross-linking of I121C and A197C. It is important to note that, while homomeric S1-I121C/S1-I121C cross-linking needs to be induced by $Cu(Phen)_3$ oxidation, S1-I121C of one protomer can spontaneously cross-link with S4-A197C of the other protomer in absence of oxidative treatment [Fig. 3, 0 $Cu(Phen)_3$]. This observation suggests that S1-I121C in one protomer is closer to S4-A197C in the other protomer than to the other protomer's S1-I121C. This interpretation is consistent with our homology model, in which S1-I121 and S4-A197 lie 5 Å apart, while the two S1-I121 are separated by 16 Å (*SI Appendix*, Fig. S3*E*). Interprotomer cross-linking between I121C and A197C is incompatible with the S4 dimer model (*SI Appendix*, Fig. S3*C*), thus validating the S1–S4 dimer model, with the S1 segment of one protomer interacting with the S4 segment of the other protomer in the membrane portion of the interface.

The External Transmembrane Dimer Interface Controls Channel Closure. By plotting the effects on the gating parameters of the cysteine mutations in the external half of S1 (S161 to I175), we observed a helical periodicity in the effects on the $V_{1/2}$ of the *G-V* curve and tail current decay time (Fig. 4 *A* and *B*). Cysteine mutations of S1 external interfacial residues (S161, V165, L169, and K173) slowed the tail current but cysteine mutations at other external positions either had no effect or accelerated the tail current (Fig. 4 *B–D* and Table 1). These results suggest that S1 interfacial residues exert a strong and specific influence on the stability of the Hv1 open state. Except for position S161, which starts of as serine, mutation of Interface I residues into small alanine or serine residues also strongly slowed deactivation (Fig. 4 *E–H*). This argues that slowing of deactivation by mutation to cysteine was not due to cross-linking. Consistently, except for K173C (14), no cross-linking between homologous residues (i.e., residues at the same position in both subunits) was observed on analog positions of hHv1 (A113C, L117C, and I121C) in the absence of oxidative treatment (Fig. 3 and *SI Appendix*, Fig. S4*C*) (14). To gain more insight into the mechanisms driving this control, we varied systematically the size of the amino acid side chain at four of these S1 positions: 161, 165, 169, and 173. Except for S161, we observed a strong correlation (R^2 0.949 to 0.999, linear fit) between the volume of the amino acid side chain and the tail decay time, with smaller amino acids (e.g., alanine, serine, or cysteine) slowing channel deactivation, while bigger amino acids (e.g., tryptophan) accelerated deactivation (Fig. 4 *C* and *E–H*). This suggests that the stability of the open state, as reflected by the kinetics of channel deactivation, is controlled by steric repulsion between the extracellular half of S1 and its partner on the other subunit.

In our homology model, Interface I residues interact with the S3–S4 loop and the extracellular end of the S4 segment of the other protomer (Region II in Fig. 2*D*). In particular, S1 residues S161, V165, and L169 were predicted to interact with L256, I253, and L250 in the S4 helix (Fig. 2*D*). We therefore examined the effect of cysteine and alanine mutations of these S4 residues. We found that these S4 mutations induced functional effects similar to the cysteine and alanine mutations of the S1 Interface I residues: Slowing of the deactivation kinetics (2.4- to 12-fold increase in tail decay time compared to WT) (Fig. 5 *A* and *B* and *SI Appendix*, Table S1), as well a shift of the *G-V* curve to the left ($\Delta V_{1/2} = -10$ to -48 mV) (*SI Appendix*, Table S1). As in S1, the fact that both cysteine and alanine substitutions induce similar functional effects suggests that the effect of S4 cysteine mutations is not due to disulfide bridging. This interpretation is consistent with the lack in previous studies of cross-linking between homologous residues of S4 positions L250, I253, and L256 in the absence of oxidative treatment (26).

To test if S1 and S4 residues control channel closure through the same mechanism, we made double mutants combining cysteine mutations at one of the S1 positions and one the S4 positions. Except for S1-L169C, which could make disulfide bonds with S4-A247C, and to a lower extent with S4-G199C and -L250C (see above), we did not observe any heterologous cross-linking with other S1–S4 double cysteine mutant combinations, even after treatment with $Cu(Phen)_3$ (*SI Appendix*, Fig. S4*C*). This is probably because they are buried inside the membrane, and thus inaccessible to endogenous oxygen. However, S1–S4 double cysteine mutants strongly affected channel function. Most of these mutants were either always open at -80 mV, or their closure following a step from +60 to -80 mV too slow to measure. We therefore turned to a more hyperpolarized holding potential of -120 mV, and measured the tail currents from a step to +20 mV. We focused on one pair of residues, S161 in S1 and I253 in S4, for which tail decay times were fast enough to be measured. With closure rates of Hv1-S161C and

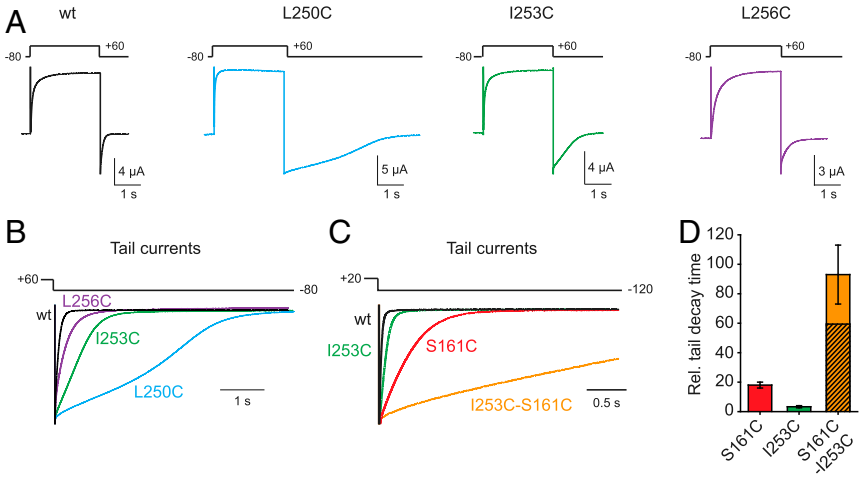

Fig. 5. Putative partners of S1 interfacial residues on S4 also exert a strong control on channel closure. (*A*) Representative current traces for a voltage step to +60 mV of oocytes expressing CiHv1 channels containing a cysteine mutation at S4 positions L250, I253, and L256. (*B*) Superposition of the normalized tail currents of WT (black), L250C (blue), and L256C (purple) channels. Note the slowing of the tail currents compared to WT channels. (*C*) Superposition of the normalized tail currents of WT, S161C (red), I253C (green), and S161C-I253C (yellow) channels from a +20 to -120 mV voltage step. (*D*) Relative tail decay times of S161C ($n = 6$), I253C ($n = 8$), and S161C-I253C ($n = 7$) mutants. The hashed bar indicates the theoretical tail decay time of S161C-I253C mutant, had the two mutations been independent.

Hv1-I253C being 18-fold and 3.3-fold slower than WT, respectively, we predicted that closure of the double-mutant S161C/I253C would be ~59-fold slower than WT if the effects of the two mutations were independent (hashed bar in Fig. 5*D*). Closure of Hv1-S161C-I253C was 1.5-fold slower than the independence prediction (relative tail decay time = 90 ± 20 s, $n = 7$) (Fig. 5 *C* and *D*), suggesting that there is a positive synergy between the S161C and I253C mutations. These results, together with our modeling and cross-linking results, are in favor of cooperative action at the dimer interface to control channel closure by Interface I residues on S1 and L250, I253, and L256 on S4.

Discussion

S1 and S4 Form the Dimer Interface. While it has been known that Hv1 subunits dimerize through their C-terminal coiled-coil domain intracellularly (12, 13, 28), how these subunits interact in their transmembrane part has been under debate. Using mutagenesis, electrophysiology, biochemistry, and modeling, we provide an experimental validation of a transmembrane dimer interface involving interactions between S1 and S4. We propose a molecular model of an Hv1 dimer that matches very well experimental data of ours and others (26, 38). In its extracellular part, the dimer interface mainly involves the two S1 segments. In its transmembrane portion, it involves both S1 and S4 segments, the S4 segment of one subunit interacting with the S1 and S4 segments of the other subunit. In the dimer model we generated, based on the crystal structures of two mHv1-CiVSP chimera monomers, the intracellular part of the transmembrane interface was mainly formed by S4–S4 interactions. However, our results and a recent NMR structure of hHv1 VSD (25) suggest that the intracellular part of S1 might also be involved in the interface, probably in some, but not all gating states.

Architecture of the Hv1 transmembrane dimer interface was previously investigated by Western blot analysis of cysteine–cysteine cross-linkings (26, 38). However, given the lack of structural information and the high number of residue couples to test for cysteine substitution, only cross-linkings between homologous residues (i.e., residues at the same position in both subunits) were made. These studies therefore yielded an incomplete picture of the dimer interface. The great power of functional mutagenesis scanning is that it allows probing of the environment and structure of proteins ab initio (i.e., without prior structural knowledge) (33, 34, 39, 40). For example, tryptophan and alanine scanning were used to determine the relative arrangements of the VSD and pore domain segments in voltage-gated potassium channels (34, 39, 40) before the first crystal structures for these channels were released (41, 42). In this work, we made an adaptation of this assay by analyzing the differences between the scanning results in the dimer and in the monomer, thus identifying the residues of the S1 segment that shift from a putative protein to a putative lipid environment during monomerization. Because this assay relies on electrophysiology of channels expressed at the plasma membrane, as opposed to most biochemistry experiments probing the total protein content of the cell, including immature proteins retained in the endoplasmic reticulum, we believe that the architecture of the Hv1 dimer interface that we propose reflects the one of mature, membrane-expressed, functional channels. In an additional effort to selectively target membrane-expressed channels, cross-linkings for Western blot analysis were induced by treatment with membrane impermeant copper phenanthroline on intact cells rather than on membrane extracts. We found that the dimer interface not only involved S1 external tips, but that it also extended through the whole length of the S1 segment down to its intracellular part, something that was never shown before. Indeed, Western blot and double mutant cycle analysis revealed that transmembrane S1 interfacial residues interacted with the S4 segment, hence explaining why these residues had not been previously identified.

While being a powerful technique to investigate the environment of residues in structured protein regions, such as α-helices or β-sheets, mutagenesis scanning is much more limited to characterize flexible elements, such as residues with variable orientations during the gating process or loops, which are more tolerant to amino acid substitutions. Accordingly, while our observations point to S161 and V165 positioning at the dimer interface, the results of the scan were more subject to interpretation for S1 extremities, which are more likely to be flexible. Extracellularly, L169 appeared as noninterfacial in our scan because its mutation had a functional impact in both the monomer and the dimer. However, disulfide cross-linking revealed that it was part of the dimer interface. L169C mutation could make either homologous (L169C-L169C) or heterologous cross-links with S4-A247C, suggesting that this residue can indeed change orientation during gating. Conversely, V174 and I175, which were shown to cross-link in human and mouse Hv1 (14, 26), did not come out as interfacial residues in our assay because cysteine mutation at these positions altered channel function neither in the dimer nor in the monomer. Mutagenesis scanning and disulfide cross-linking are therefore two complementary methods required to give a complete picture of an interface. Finally, it is interesting to note that cysteine mutation at positions V157 and V164 perturbed channel function in the monomer, but not the dimer (Table 1). Residues V157 and V164 were shown to be part of the two hydrophobic layers constricting the inner VSD water-filled crevice (24, 35), the opening of which seems to be required to allow proton permeation (35, 43). This suggests that at least two parameters control channel opening: The interprotomer interface (see below) and the intraprotomer hydrophobic layers. In the dimer, rearrangements of the interprotomer interface are likely to be rate-limiting. In absence of these interactions in the monomer, rearrangements of intraprotomer hydrophobic layers become rate-limiting, likely leading to a stronger effect of V157C and V164C in the monomer.

The Transmembrane Dimer Interface Modulates Deactivation. Opening and closure of Hv1 dimers is highly cooperative (20, 27). This cooperativity was proposed to involve the coiled-coil domains (28, 36). By making a continuous helix from the S4 segments (26), the coiled-coiled domain has been proposed to couple the motions of the two voltage sensors (28), although direct evidence for such S4–S4 coupling is lacking. We show that the VSDs also make extensive interactions involving the whole S1 segments, which contain part of the selectivity filter (22, 23) and were proposed to act as the gate (21). Our results therefore imply that cooperative gating can also be mediated by direct interactions between the two gates. This is consistent with the observation that cooperative binding of some Hv1 open channel blockers depended on S1–S1 interactions, but not on the coiled-coil domain (32). Our model and observations suggest that the voltage-dependent motions of the S1 and S4 segment of one subunit could directly influence the motions of both the S1 and S4 segments of the other subunit. Accordingly, we showed that the transmembrane dimer interface played a very strong role in the control of Hv1 gating, especially on the deactivation step. Further investigation is required, however, to demonstrate actual cross-talk between the S1–S4 portions of the two protomers. At the most external S1 positions V165, L169, and K173, open-state stability was controlled by steric repulsions between these S1 residues and their partners (likely both the S1 and S4 residues) (Figs. 3 and 4) on the other subunit. This suggests that the extracellular regions of the two VSDs get closer together upon channel activation, consistent with previous data showing that S1 outer ends are closer in the open state (21, 32).

Finally, the fact that perturbations at the level of Hv1 dimer interface can induce bidirectional effects (stabilization or destabilization of the open state) depending on the nature of the perturbation could pave the way for the development of new

modulators. Despite recent advancements in Hv1 pharmacology (44–47), most Hv1 modulators have poor selectivity. Targeting this dimer interface, which does not exist in other voltage-gated ion channels, should allow design of modulators more selective for this class of channels involved in numerous pathologies ranging from cancer, neuronal death and infertility.

Methods

Mutagenesis and Expression in *Xenopus* Oocytes. Female *Xenopus laevis* animals were housed and surged according to the guidelines of Berkeley's Animal Care and Use Committee (Animal Use Protocol R187-0814). CiHv1 mutants were constructed via site-directed mutagenesis in the pSD64TF vector (16) using Quikchange mutagenesis (Stratagene) and verified by sequencing. DNA was linearized with SbfI or SacI and transcribed to RNA using the SP6 mMessage mMachine Kit (Ambion). *X. laevis* oocytes were injected with 50 nL of RNA at a concentration of 0.5 to 2 μg/μL and incubated at 18 °C for 1 to 5 d in ND96 (96 mM NaCl, 2 mM KCl, 1.8 mM $CaCl_2$, 1 mM $MgCl_2$, 10 mM Hepes, 5 mM pyruvate, and 100 mg/L gentamycin, pH adjusted to 7.6 with NaOH) or in Barth's solution [88 mM NaCl, 1 mM KCl, 0.33 mM $Ca(NO_3)_2$, 0.41 mM $CaCl_2$, 0.82 mM $MgSO_4$, 2.4 mM $NaHCO_3$, 10 mM Hepes, and 100 mg/L gentamycin, pH adjusted to pH 7.6 with NaOH].

TEVC Recordings Recordings. TEVC recordings were done with either a Dagan CA-1 (Dagan) or an oocyte clamp OC-725C (Warner Instruments) amplifier. An Axon Digidata-1440 board and the software suite pClamp10 (Molecular Devices) were used to control the amplifiers and collect data. TEVC recordings were adapted from different protocols (20, 27). To minimize pH changes due to proton efflux, high buffer solutions (100 mM Hepes) were used both intra- and extracellularly. On the day of the experiment, oocytes were injected with 50 nL of a solution of 1 M of 2-(4-(2-hydroxyethyl)piperazin-1-yl)ethanesulfonic acid (Hepes) at pH 7.0 (pH adjusted to 7.0 with KOH) and left 1 to 2 h at 18 °C to recover in the extracellular recording solution. This results in ∼100 mM Hepes in the cytosol (20, 27). The extracellular recording solution contained: 46 mM NaCl, 1 mM KCl, 1 mM $MgCl_2$, 1 mM $CaCl_2$, 100 mM Hepes, pH adjusted to 7.5 with NaOH. Unless otherwise noted, holding potential was −80 mV. Currents were leak-subtracted off line, assuming ohmic leak and using currents from potentials between −80 and −40 mV.

Data Analysis and Statistics. All of the values in the paper represent average values. Error bars represent the SEM; "*n*" represents the number of oocytes tested. Data were collected on at least 2 different experimental days, on oocytes obtained from at least two different *Xenopus*. Before running statistical tests, sample distributions were tested for normality using the Kolmogorov–Smirnov test. All Student's and paired *t* tests are two-sided, with samples considered of unequal variance.

Data were analyzed using Clampfit (Molecular Devices), Igor Pro (WaveMetrics), and SigmaPlot (Systat Software) softwares. Unless otherwise specified, *G-V* curves were calculated from the tail current amplitudes at −80 mV. *G-V* curves were fitted using the Boltzmann equation: $G/G_{max} = 1/(1 + \exp(-(V - V_{1/2})/B)$, where B represents the Boltzmann factor kT/ze_0, which is inversely proportional to the slope of the *G-V* curve; and $V_{1/2}$ is the voltage at which half of the channels are open. Activation and deactivation time constants were determined by fitting the current traces with a biexponential function in the form: $I = A_{fast} \times \exp(-t/\tau_{fast}) + A_{slow} \times \exp(-t/\tau_{slow})$, where τ_{fast} and τ_{slow} represent the time constants of the fast and the slow components, respectively, and A_{fast} and A_{slow} the amplitudes of the fast and slow components, respectively. In Table 1 we report the weighted activation and deactivation time constants [$\tau_w = (A_{fast} \times \tau_{fast} + A_{slow} \times \tau_{slow})/(A_{fast} + A_{slow})$] as a global measure of the activation kinetics of the different constructs. Some CiHv1 mutants with slow deactivation kinetics had tails with a bumpy shape (possibly due to imperfect pH buffering or clamping) that made it difficult to fit them. To quantify the rate of tail current decrease, we thus measured for all of the dimeric constructs the tail decay time, defined as the time necessary for current to decay from 90 to 10% of their initial amplitude following repolarization from to −80 mV.

Cysteine Scanning Functional Assay. For each cysteine mutant, we measured the $V_{1/2}$ and slope of their *G-V* curve, as well as the weighted activation time constant and the weighted deactivation time constant (monomers) or tail decay time (dimers) for a step from −80 to +60 mV and back to −80 mV. Due to a strong day-to-day variability, we always compared the parameters of the different mutants to the parameters of the WT channels obtained on the same experimental day. For each day, we normalized the gating parameters of each mutant cell to the average of the corresponding gating parameter of the control (Hv1wt or Δ*N*-Hv1-ΔC): For each mutant cell, $\Delta V_{1/2}$[or ΔB] = $V_{1/2}$[or B]$_{mutant}$ − average($V_{1/2}$[or B]$_{control}$; mutant/WT kinetics = τ_w[or tail decay time]$_{mutant}$/average(τ_w[or tail decay time]$_{control}$). Numbers represented in Table 1 represent the means and SEs of the normalized gating parameters. Because of this day-to-day variability, the threshold values to consider that the mutation as an impact were: A shift of $V_{1/2}$ by at least 10 mV; a shift of Boltzmann factor by at least 5 mV; a change in weighted activation time constant, in weighted deactivation time constant or tail decay time by at least threefold.

Western Blot Analysis. *Xenopus* oocytes were injected with 50 nL of the mRNA coding for the GFP-tagged construct of interest at 0.3 μg/μL, or with a 1:1 mixture of mRNAs coding GFP-tagged and untagged subunits at 0.3 μg/μL. After 36 to 48 h of expression, oocytes were divided in two groups. The first group was left untreated [0 $Cu(Phen)_3$]. The second group was incubated 1 h at room temperature in a Barth solution (48) with 300 μM $Cu(Phen)_3$ (per 1 mL solution, 3 μL of 100 mM $CuSO_4$ stock solution in H_2O, and 3 μL of 350 mM ortho-phenanthroline stock solution in ethanol, 1 mL solution per five oocytes), then washed three times in Barth. Five oocytes of each group were homogenized on ice by back and forth pipetting with 125 μL of lysis buffer (20 mM Tris pH 8.0, 150 mM NaCl, 1 mM EDTA, 1% *N*-dodecyl-β-D-maltoside [DDM], 1 mM NEM, 1/20 of a complete protease inhibitor mixture tablet, Roche Complete, Mini) until a homogenous suspension was obtained. Samples were then centrifuged (15,000 × *g* for 10 min at 4 °C). The supernatant was collected, centrifuged 10 min at 15,000 × *g* and 4 °C, and the supernatant was collected again. Total protein concentrations of the samples were measured by a Pierce BCA assay (Pierce BCA Protein Assay Kit, ThermoFisher Scientific). For all of the samples, total protein concentration was around 1 mg/mL; 33 μL of the purified sample was added to 66 μL of loading buffer (200 mM Tris pH 6.8, 30% glycerol, 4% SDS, ∼20 μM bromophenol blue), boiled at 95 °C during 5 min, then cooled on ice. In the reducing conditions, 10% (vol/vol) β-mercaptoethanol (βME) was added to the loading buffer.

Samples were separated on 12% or 4 to 15% SDS/PAGE gradient gels (∼5 μg total protein per lane), transferred to polyvinylidene difluoride (PVDF) membranes, and immunoblotted with anti-GFP antibody (1:1,000, rabbit GFP polyclonal antibody, Invitrogen catalog number #A-11122). Protein bands were visualized using secondary goat peroxidase-linked anti-rabbit antibodies (1:10,000, Jackson Immuno Research catalog #111-035-003), with the SuperSignal West Pico Chemiluminescent substrate (ThermoFisher Scientific).

Modeling and Structure Illustration. Homology models of CiHv1 VSD were produced with the Modeler module of Biovia Discovery Studio (Dassault Systèmes), using the alignment in *SI Appendix*, Fig. S3*A* and either the crystal structure of mHv1cc [PDB ID code 3WKV (24)] or the NMR structure of hHv1 VSD [PDB ID code 5OQK (25)] as templates. Models with the lowest PDF energy were chosen. The homology model of a CiHv1 dimer was produced using MODELLER (49). The template was made by superposing the crystal structure of two mHv1cc chimeras [PDB ID code 3WKV (24)] and the crystal structure of the dimeric coiled-coil domain of mHv1 [PDB ID code 3VMX, (28)] according to the alignment in *SI Appendix*, Fig. S1*F*. A helical constraint was applied to the residues of the S4 and S4 to coiled-coil linker to maintain helical continuity between S4 and the coiled-coil domain. Structure representations were prepared with Biovia Discovery Studio 4.1 (Dassault Systems).

Data Availability. All study data are included in the article and *SI Appendix*.

ACKNOWLEDGMENTS. We thank Y. Okamura (Osaka University) for the cDNA of *Ciona intestinalis* Hv1; Hitomi Otsuki-Okada, Cherise Stanley (University of California, Berkeley), and Mélissa David (Institut de Biologie de l'Ecole Normale Supérieure, Paris) for help with the cloning; as well as the members of the E.Y.I. laboratory and Paoletti laboratory (Institut de Biologie de l'Ecole Normale Supérieure) for discussion. This work was supported by Labex Memolife (postdoctoral fellowship to L.M.); the European Commission Marie Sklodowska-Curie fellowship H2020-MSCA-IF- 2015 Grant #701467 (to L.M.); INSERM (L.M.); and National Institutes of Health Grant R01 NS35549 (to L.M. and E.Y.I.).

1. A. Roos, W. F. Boron, Intracellular pH. *Physiol. Rev.* **61**, 296–434 (1981).
2. T. E. DeCoursey, Voltage-gated proton channels: Molecular biology, physiology, and pathophysiology of the H(V) family. *Physiol. Rev.* **93**, 599–652 (2013).
3. T. E. Decoursey, Voltage-gated proton channels and other proton transfer pathways. *Physiol. Rev.* **83**, 475–579 (2003).
4. T. Seredenina, N. Demaurex, K. H. Krause, Voltage-gated proton channels as novel drug targets: From NADPH oxidase regulation to sperm biology. *Antioxid. Redox Signal.* **23**, 490–513 (2015).
5. M. Capasso, T. E. DeCoursey, M. J. Dyer, pH regulation and beyond: unanticipated functions for the voltage-gated proton channel, HVCN1. *Trends Cell Biol.* **21**, 20–28 (2011).

6. I. S. Ramsey, E. Ruchti, J. S. Kaczmarek, D. E. Clapham, Hv1 proton channels are required for high-level NADPH oxidase-dependent superoxide production during the phagocyte respiratory burst. *Proc. Natl. Acad. Sci. U.S.A.* **106**, 7642–7647 (2009).
7. L. J. Wu *et al*., The voltage-gated proton channel Hv1 enhances brain damage from ischemic stroke. *Nat. Neurosci.* **15**, 565–573 (2012).
8. Y. Wang, S. J. Li, X. Wu, Y. Che, Q. Li, Clinicopathological and biological significance of human voltage-gated proton channel Hv1 protein overexpression in breast cancer. *J. Biol. Chem.* **287**, 13877–13888 (2012).
9. E. Hondares *et al*., Enhanced activation of an amino-terminally truncated isoform of the voltage-gated proton channel HVCN1 enriched in malignant B cells. *Proc. Natl. Acad. Sci. U.S.A.* **111**, 18078–18083 (2014).
10. P. V. Lishko, I. L. Botchkina, A. Fedorenko, Y. Kirichok, Acid extrusion from human spermatozoa is mediated by flagellar voltage-gated proton channel. *Cell* **140**, 327–337 (2010).
11. F. Tombola, M. M. Pathak, E. Y. Isacoff, How does voltage open an ion channel? *Annu. Rev. Cell Dev. Biol.* **22**, 23–52 (2006).
12. H. P. Koch *et al*., Multimeric nature of voltage-gated proton channels. *Proc. Natl. Acad. Sci. U.S.A.* **105**, 9111–9116 (2008).
13. F. Tombola, M. H. Ulbrich, E. Y. Isacoff, The voltage-gated proton channel Hv1 has two pores, each controlled by one voltage sensor. *Neuron* **58**, 546–556 (2008).
14. S. Y. Lee, J. A. Letts, R. Mackinnon, Dimeric subunit stoichiometry of the human voltage-dependent proton channel Hv1. *Proc. Natl. Acad. Sci. U.S.A.* **105**, 7692–7695 (2008).
15. I. S. Ramsey, M. M. Moran, J. A. Chong, D. E. Clapham, A voltage-gated proton-selective channel lacking the pore domain. *Nature* **440**, 1213–1216 (2006).
16. M. Sasaki, M. Takagi, Y. Okamura, A voltage sensor-domain protein is a voltage-gated proton channel. *Science* **312**, 589–592 (2006).
17. S. Y. Lee, J. A. Letts, R. MacKinnon, Functional reconstitution of purified human Hv1 H+ channels. *J. Mol. Biol.* **387**, 1055–1060 (2009).
18. E. M. Carmona *et al*., Gating charge displacement in a monomeric voltage-gated proton (H_v1) channel. *Proc. Natl. Acad. Sci. U.S.A.* **115**, 9240–9245 (2018).
19. C. Gonzalez, S. Rebolledo, M. E. Perez, H. P. Larsson, Molecular mechanism of voltage sensing in voltage-gated proton channels. *J. Gen. Physiol.* **141**, 275–285 (2013).
20. C. Gonzalez, H. P. Koch, B. M. Drum, H. P. Larsson, Strong cooperativity between subunits in voltage-gated proton channels. *Nat. Struct. Mol. Biol.* **17**, 51–56 (2010).
21. L. Mony, T. K. Berger, E. Y. Isacoff, A specialized molecular motion opens the Hv1 voltage-gated proton channel. *Nat. Struct. Mol. Biol.* **22**, 283–290 (2015).
22. T. K. Berger, E. Y. Isacoff, The pore of the voltage-gated proton channel. *Neuron* **72**, 991–1000 (2011).
23. B. Musset *et al*., Aspartate 112 is the selectivity filter of the human voltage-gated proton channel. *Nature* **480**, 273–277 (2011).
24. K. Takeshita *et al*., X-ray crystal structure of voltage-gated proton channel. *Nat. Struct. Mol. Biol.* **21**, 352–357 (2014).
25. M. Bayrhuber *et al*., Nuclear magnetic resonance solution structure and functional behavior of the human proton channel. *Biochemistry* **58**, 4017–4027 (2019).
26. Y. Fujiwara, T. Kurokawa, Y. Okamura, Long α helices projecting from the membrane as the dimer interface in the voltage-gated H(+) channel. *J. Gen. Physiol.* **143**, 377–386 (2014).
27. F. Tombola, M. H. Ulbrich, S. C. Kohout, E. Y. Isacoff, The opening of the two pores of the Hv1 voltage-gated proton channel is tuned by cooperativity. *Nat. Struct. Mol. Biol.* **17**, 44–50 (2010).
28. Y. Fujiwara *et al*., The cytoplasmic coiled-coil mediates cooperative gating temperature sensitivity in the voltage-gated H(+) channel Hv1. *Nat. Commun.* **3**, 816 (2012).
29. H. Okuda, Y. Yonezawa, Y. Takano, Y. Okamura, Y. Fujiwara, Direct interaction between the voltage sensors produces cooperative sustained deactivation in voltage-gated H+ channel dimers. *J. Biol. Chem.* **291**, 5935–5947 (2016).
30. Q. Li *et al*., Structural mechanism of voltage-dependent gating in an isolated voltage-sensing domain. *Nat. Struct. Mol. Biol.* **21**, 244–252 (2014).
31. Q. Li *et al*., Resting state of the human proton channel dimer in a lipid bilayer. *Proc. Natl. Acad. Sci. U.S.A.* **112**, E5926–E5935 (2015).
32. L. Hong, V. Singh, H. Wulff, F. Tombola, Interrogation of the intersubunit interface of the open Hv1 proton channel with a probe of allosteric coupling. *Sci. Rep.* **5**, 14077 (2015).
33. S. Choe, C. F. Stevens, J. M. Sullivan, Three distinct structural environments of a transmembrane domain in the inwardly rectifying potassium channel ROMK1 defined by perturbation. *Proc. Natl. Acad. Sci. U.S.A.* **92**, 12046–12049 (1995).
34. S. A. Monks, D. J. Needleman, C. Miller, Helical structure and packing orientation of the S2 segment in the Shaker K+ channel. *J. Gen. Physiol.* **113**, 415–423 (1999).
35. A. Chamberlin *et al*., Hydrophobic plug functions as a gate in voltage-gated proton channels. *Proc. Natl. Acad. Sci. U.S.A.* **111**, E273–E282 (2014).
36. F. Qiu, S. Rebolledo, C. Gonzalez, H. P. Larsson, Subunit interactions during cooperative opening of voltage-gated proton channels. *Neuron* **77**, 288–298 (2013).
37. I. B. Afanas'ev, *Superoxide Ion: Volume II (1991): Chemistry and Biological Implications*, (CRC Press, 2017).
38. S. Y. Lee, A. Banerjee, R. MacKinnon, Two separate interfaces between the voltage sensor and pore are required for the function of voltage-dependent K(+) channels. *PLoS Biol.* **7**, e47 (2009).
39. Y. Li-Smerin, D. H. Hackos, K. J. Swartz, A localized interaction surface for voltage-sensing domains on the pore domain of a K+ channel. *Neuron* **25**, 411–423 (2000).
40. Y. Li-Smerin, D. H. Hackos, K. J. Swartz, alpha-helical structural elements within the voltage-sensing domains of a K(+) channel. *J. Gen. Physiol.* **115**, 33–50 (2000).
41. S. B. Long, E. B. Campbell, R. Mackinnon, Crystal structure of a mammalian voltage-dependent Shaker family K+ channel. *Science* **309**, 897–903 (2005).
42. S. B. Long, X. Tao, E. B. Campbell, R. MacKinnon, Atomic structure of a voltage-dependent K+ channel in a lipid membrane-like environment. *Nature* **450**, 376–382 (2007).
43. R. Banh *et al*., Hydrophobic gasket mutation produces gating pore currents in closed human voltage-gated proton channels. *Proc. Natl. Acad. Sci. U.S.A.* **116**, 18951–18961 (2019).
44. L. Hong, I. H. Kim, F. Tombola, Molecular determinants of Hv1 proton channel inhibition by guanidine derivatives. *Proc. Natl. Acad. Sci. U.S.A.* **111**, 9971–9976 (2014).
45. L. Hong, M. M. Pathak, I. H. Kim, D. Ta, F. Tombola, Voltage-sensing domain of voltage-gated proton channel Hv1 shares mechanism of block with pore domains. *Neuron* **77**, 274–287 (2013).
46. D. Tang *et al*., Scorpion toxin inhibits the voltage-gated proton channel using a Zn^{2+}-like long-range conformational coupling mechanism. *Br. J. Pharmacol.* **177**, 2351–2364 (2020).
47. R. Zhao *et al*., Role of human Hv1 channels in sperm capacitation and white blood cell respiratory burst established by a designed peptide inhibitor. *Proc. Natl. Acad. Sci. U.S.A.* **115**, E11847–E11856 (2018).
48. L. Mony, S. Zhu, S. Carvalho, P. Paoletti, Molecular basis of positive allosteric modulation of GluN2B NMDA receptors by polyamines. *EMBO J.* **30**, 3134–3146 (2011).
49. B. Webb, A. Sali, Protein structure modeling with MODELLER. *Methods Mol. Biol.* **1654**, 39–54 (2017).
50. F. M. Richards, Areas, volumes, packing and protein structure. *Annu. Rev. Biophys. Bioeng.* **6**, 151–176 (1977).